



Assembly of Tetraspanin-enriched macromolecular complexes contains membrane damage to facilitate repair

Yuwei Huang¹, Xing Zhang², Hong-Wei Wang¹ and Li Yu¹✉

Various mechanisms contribute to membrane repair^{1–8} but the machinery that mediates the repair of large wounds on the plasma membrane is less clear. We found that shortly after membrane damage, Tetraspanin-enriched macromolecular complexes are assembled around the damage site. Tetraspanin-enriched macromolecular complexes are in the liquid-ordered phase and form a rigid ring around the damaged site. This restricts the spread of the damage and prevents membrane disintegration, thus facilitating membrane repair by other mechanisms. Functionally, Tetraspanin 4 helps cells mitigate damage caused by laser, detergent, pyroptosis and natural killer cells. We propose that assembly of Tetraspanin-enriched macromolecular complexes creates a physical barrier to contain membrane damage.

The plasma membrane is a barrier surrounding the cell. Various types of damage—which may be physical, chemical or biological in nature—can cause loss of integrity of the cell membrane, which will inevitably lead to the demise of the cell if not repaired. Several different mechanisms—including exocytosis, endocytosis, SYX-2-EFF-1 repair machinery and ESCRT machinery—have been shown to play essential roles in membrane repair^{1–8}. During ESCRT-mediated membrane repair, ESCRT components are recruited to the site of damage and pinch off the damaged membrane to facilitate repair in a calcium-dependent manner⁹. ESCRT-mediated membrane repair plays important roles in maintaining cell viability following diverse types of damage, including damage caused by laser, detergents, necrosis and pyroptosis^{10–12}. ESCRT is capable of repairing small patches of membrane damage of about 100 nm; however, it is less clear how larger wounds are repaired.

Tetraspanin 4 (Tspan4) is a transmembrane protein that contains four transmembrane domains. It is a member of the Tetraspanin family. Tetraspanin family members organize membranes into cholesterol-enriched membrane domains named Tetraspanin-enriched membrane microdomains (TEMs)^{13–16}, and Tetraspanins are known to affect the properties of membranes^{15,17–19}. TEMs can assemble into micrometre-sized Tetraspanin-enriched membrane macromolecular complexes (TEMAs), which are required for the formation of migrasomes²⁰. It is unknown whether assembly of TEMAs can have other functions besides mediating migrasome formation. We found that laser-based wounding of the plasma membrane leads to rapid recruitment of green fluorescent protein (GFP)-tagged Tspan4 to the edge of the damage site in multiple cell lines (Fig. 1a and Extended Data Fig. 1a). The Tspan4-GFP first appears as a series of puncta around the damaged area; Tspan4-GFP eventually forms a ring-like structure surrounding the damage site (Fig. 1b and Supplementary Video 1). The recruitment of Tspan4-GFP seems to be specific, as membrane proteins such as

Na/K ATPase are not recruited to the damage site (Extended Data Fig. 1b). Other forms of damage—localized addition of detergent (Fig. 1c,d) and damage caused by natural killer cells (Fig. 1e)—also lead to recruitment of Tspan4 proteins to the damage site. The recruitment of Tspan4-GFP becomes visible gradually, starting at around 50 s after damage and reaching the maximum intensity at about 200 s (Fig. 1f,g and Supplementary Videos 2,3). Membrane damage was indicated by an influx of propidium iodide (PI), which showed that the wound was still open at 2 min, consistent with the recruitment timescale of Tspan4-GFP and ESCRTs (Extended Data Fig. 1c,d). Shrinkage of the Tspan4-GFP ring is accompanied by weaker PI signals, which suggests that the membrane damage has been repaired (Fig. 1f).

Next, we investigated the relationship between Tetraspanins and the ESCRT complex. We found that Tspan4-GFP partially co-localizes with various ESCRT components, including Chmp4b, Vps4a and Chmp3 (Fig. 2a). Tspan4-GFP forms a relatively smooth ring tightly enclosing the damage site, whereas ESCRT components form puncta around the damage site, with the highest density on the Tspan4-GFP⁺ area (Fig. 2b). Time-lapse imaging revealed that recruitment of Tspan4-GFP occurs almost simultaneously with the recruitment of the ESCRT component Chmp4b. After 5 min, the Chmp4b signal became weaker, whereas the Tspan4-GFP signal continued to slowly increase after the disappearance of Chmp4b (Fig. 2c). Using structured illumination microscopy (SIM), we observed the Chmp4b signals in close proximity to, but not totally colocalized with, Tspan4 after photodamage and detergent-induced damage (Fig. 2d and Extended Data Fig. 2a). These observations suggest that Tspan4 and Chmp4b are not recruited to the exact same location.

We then tested whether Tspan4 recruitment is dependent on calcium. Tspan4 was still recruited to the damage site in cells treated with the calcium chelator BAPTA-AM, which suggestss that Tspan4 contributes to membrane repair in a calcium-independent manner (Extended Data Fig. 2b). We next investigated whether the recruitment of Tspan4 and Chmp4b are dependent on each other. Overexpression of a dominant-negative Vps4a mutant or a Chmp3 mutant¹⁰ (Fig. 2e and Extended Data Fig. 2c) and knockout (KO) of Chmp4b (Fig. 2f and Extended Data Fig. 2d), which have been shown to inhibit ESCRT III activity, did not affect the recruitment of Tspan4-GFP. This suggests that ESCRT III activity is not required for the recruitment of Tspan4. Interestingly, we found that overexpression of Tspan4-GFP dramatically reduced the area around the damage site that was positive for Chmp4b puncta. In Tspan4-GFP-expressing cells, Chmp4b puncta are restricted to an area immediately surrounding the Tspan4-GFP signal, whereas in control cells, Chmp4b puncta quickly expand

¹The State Key Laboratory of Membrane Biology; Tsinghua-Peking Joint Center for Life Sciences; Beijing Frontier Research Center for Biological Structures; School of Life Science, Tsinghua University, Beijing, China. ²Ministry of Education Key Laboratory of Protein Sciences; Tsinghua-Peking Joint Center for Life Sciences; Beijing Advanced Innovation Center for Structural Biology; Beijing Frontier Research Center for Biological Structures; School of Life Science, Tsinghua University, Beijing, China. ✉e-mail: liyulab@mail.tsinghua.edu.cn

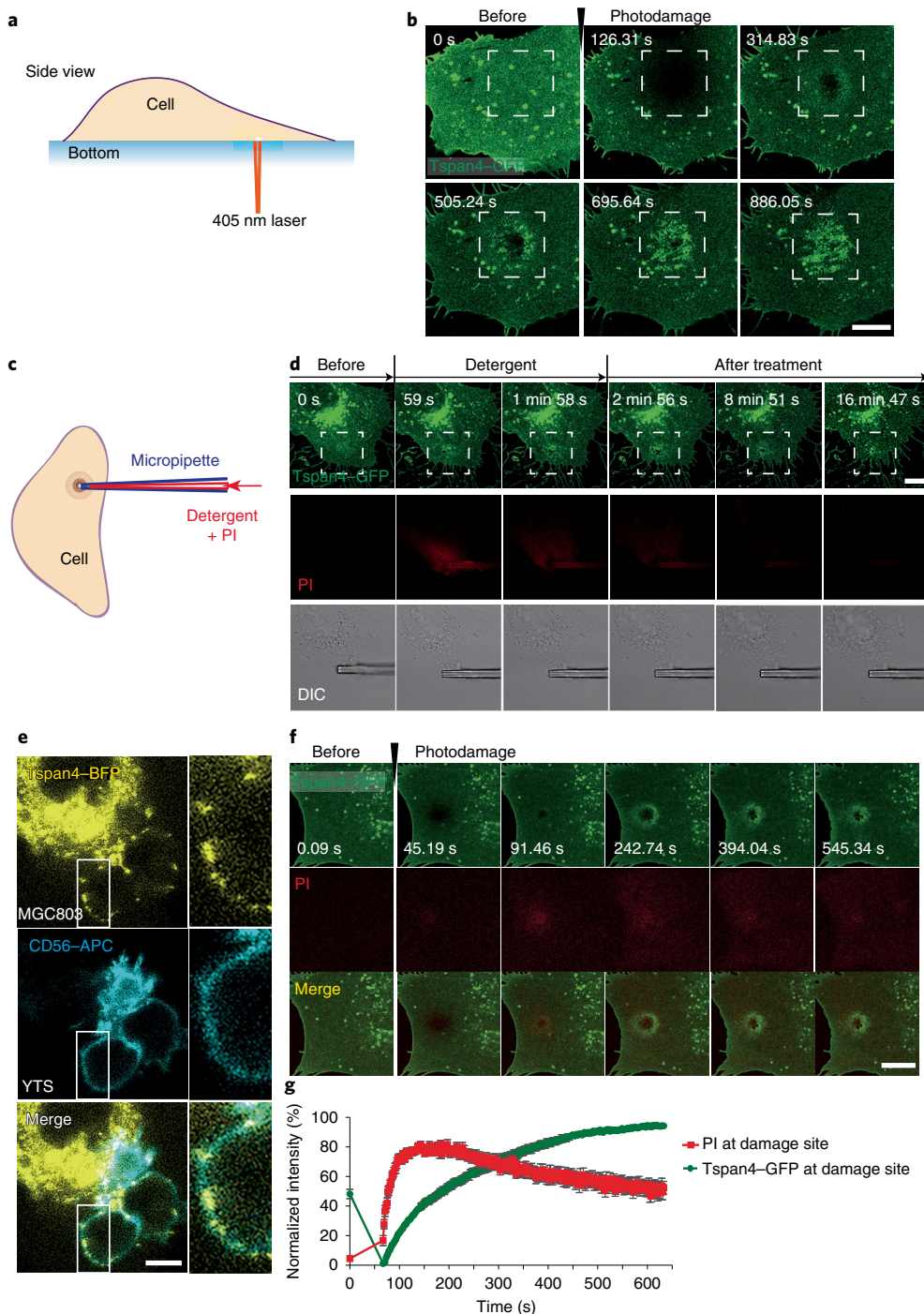


Fig. 1 | High concentrations of Tspan4 proteins are recruited to the sites of cellular membrane damage. **a**, Schematic of the photodamage assay. **b**, NRK cells overexpressing Tspan4-GFP were subjected to photodamage treatment as in **a**. Scale bar, 5 μm. White dashed boxes, damage areas. **c**, Diagram showing how cells were treated with detergent using a micropipette needle. **d**, NRK cells overexpressing Tspan4-GFP were treated with detergent using a glass micropipette needle as in **c**. DIC, differential interference contrast. White dashed boxes, damage areas. **a,d**, Time-lapse imaging was performed using confocal microscopy. **e**, MGC803 (top) cells expressing Tspan4-BFP and YTS NK (middle) cells were co-cultured and imaged using confocal microscopy (left). The YTS cells were labelled with CD56-APC. Magnified views of the regions in the white boxes are shown (right) (2.5 times magnification). **f**, Time-lapse images of NRK cells expressing Tspan4-GFP subjected to photodamage treatment. PI indicates membrane permeability. **d-f**, Scale bars, 10 μm. **g**, Normalized fluorescence intensity of Tspan4-GFP and PI at the damage site in **f**. Data are the mean ± s.e.m. of $n=21$ cells from seven independent experiments. **b,d,e**, The experiments were independently performed three times; representative images are shown.

from the damage site and occupy a much larger area (Fig. 2g-i). *Tspan4*-KO only slightly exacerbated the spread of Chmp4b puncta, which suggests that other Tetraspanins may compensate for the role of Tspan4. Similarly, overexpression of Tspan4-GFP markedly

reduced the amount of Chmp4b recruited to the damage site, whereas *Tspan4*-KO only marginally enhanced the recruitment of Chmp4b (Fig. 2h,j). Together, these data suggest that Tspan4 is not required for Chmp4b recruitment. Moreover, given that it is known

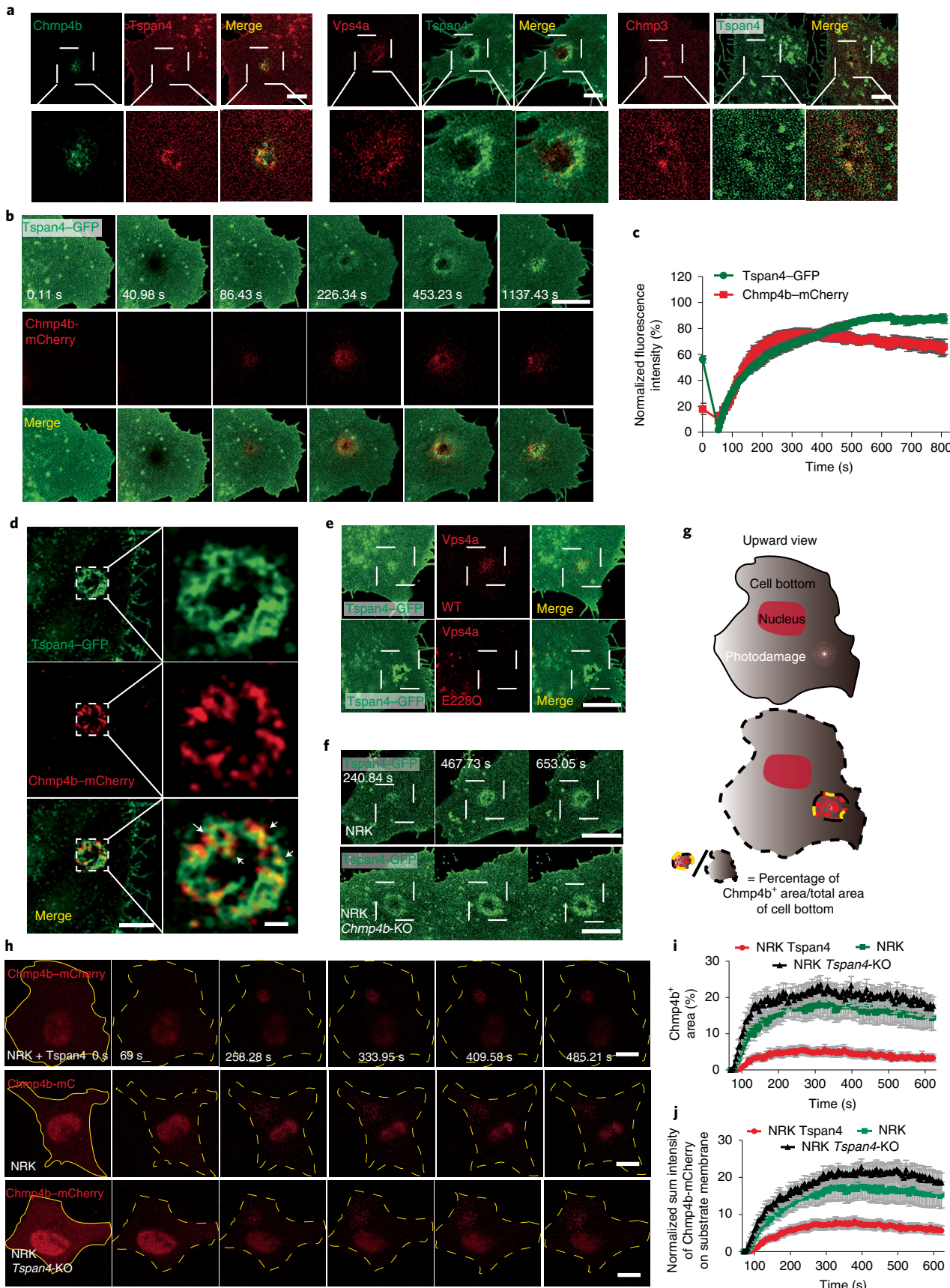


Fig. 2 | Enrichment of Tspan4 restricts the expansion of membrane damage. **a**, Chmp4b-GFP was co-expressed with Tspan4-mCherry (left), and Vps4a-mCherry (middle) and Chmp3-mCherry (right) were co-expressed with Tspan4-GFP in NRK cells. Magnified views of the boxed regions are shown (bottom) (2.5 times magnification). Scale bars, 5 μm. **b**, NRK cells co-expressing Tspan4-GFP and Chmp4b-mCherry were photodamaged and time-lapse images were collected. **c**, Cells were imaged using confocal microscopy after photodamage. **d**, Normalized fluorescence intensity of Tspan4-GFP and Chmp4b-mCherry at the sites of damage after photodamage treatment. Data are the mean ± s.e.m. of $n=36$ cells from seven independent experiments. **e**, Localization of Tspan4 and Vps4a at damage sites in cells co-expressing Tspan4-GFP and Vps4a-mCherry (top) or Vps4a E228Q-mCherry (bottom) following photodamage, analysed by confocal microscopy. White dashed boxes, damage areas. **f**, Images of Tspan4-GFP at the damage site were collected from wild-type (WT; top) and Chmp4b-KO (bottom) NRK cells after photodamage treatment. White dashed boxes, damage areas. **g**, Schematic of the method used to calculate the area positive for Chmp4b-mCherry signal on the bottom of the cell. A cell at the time of photodamage (top); cell at subsequent time points (bottom). **h**, Chmp4b-mCherry was expressed in Tspan4-overexpressing (top), WT (middle) and Tspan4-KO (bottom) NRK cells. The cells were photodamaged and monitored by time-lapse imaging. Yellow outline indicates the total area of cell bottom. **i**, Scale bars, 10 μm. **j**, Area covered by Chmp4b-mCherry⁺ signal in the images from **h**. The Chmp4b-mCherry⁺ areas were normalized to the total cell area as in **g**. **k**, Total intensity of Chmp4b-mCherry⁺ signal on the bottom of the cell. **l**, Data are the mean ± s.e.m. of $n=19$ cells from four independent experiments. **m**, The experiments were independently performed three times; representative images are shown.

that Chmp4b marks the damage site, these data also imply that over-expression of Tspan4-GFP prevents the membrane damage from spreading. These results do not rule out the possibility that other Tetraspanins may be involved in the recruitment of Chmp4b; they also do not rule out the possibility that the ESCRT machinery may affect the recruitment of other Tetraspanins as there are 33 members of the Tetraspanin family.

We investigated the mechanism by which Tspan4 mediates protection from membrane damage next. As mentioned previously, Tetraspanins on membranes organize into specialized microdomains named TEMs. We recently demonstrated that TEMs can assemble into micrometre-scale macrodomains during migrasome formation. These TEMAs have highly elevated membrane rigidity and are resistant to membrane deformation induced by mechanical force²⁰. Thus, we reasoned that Tspan4 may promote membrane repair by forming a rigid ring that surrounds the damaged area and restricts its further expansion. To investigate whether Tspan4 is recruited to damage sites in the form of TEMs, we checked a series of TEM-enriched molecules, including other Tetraspanins and Integrin-α5. We found that all of these molecules are recruited to the damage sites (Fig. 3a). In addition to proteins, cholesterol is an essential component of TEMs, and formation of TEMAs is dependent on cholesterol. We thus tested whether cholesterol is required for assembly of the TEMA ring and found that cholesterol

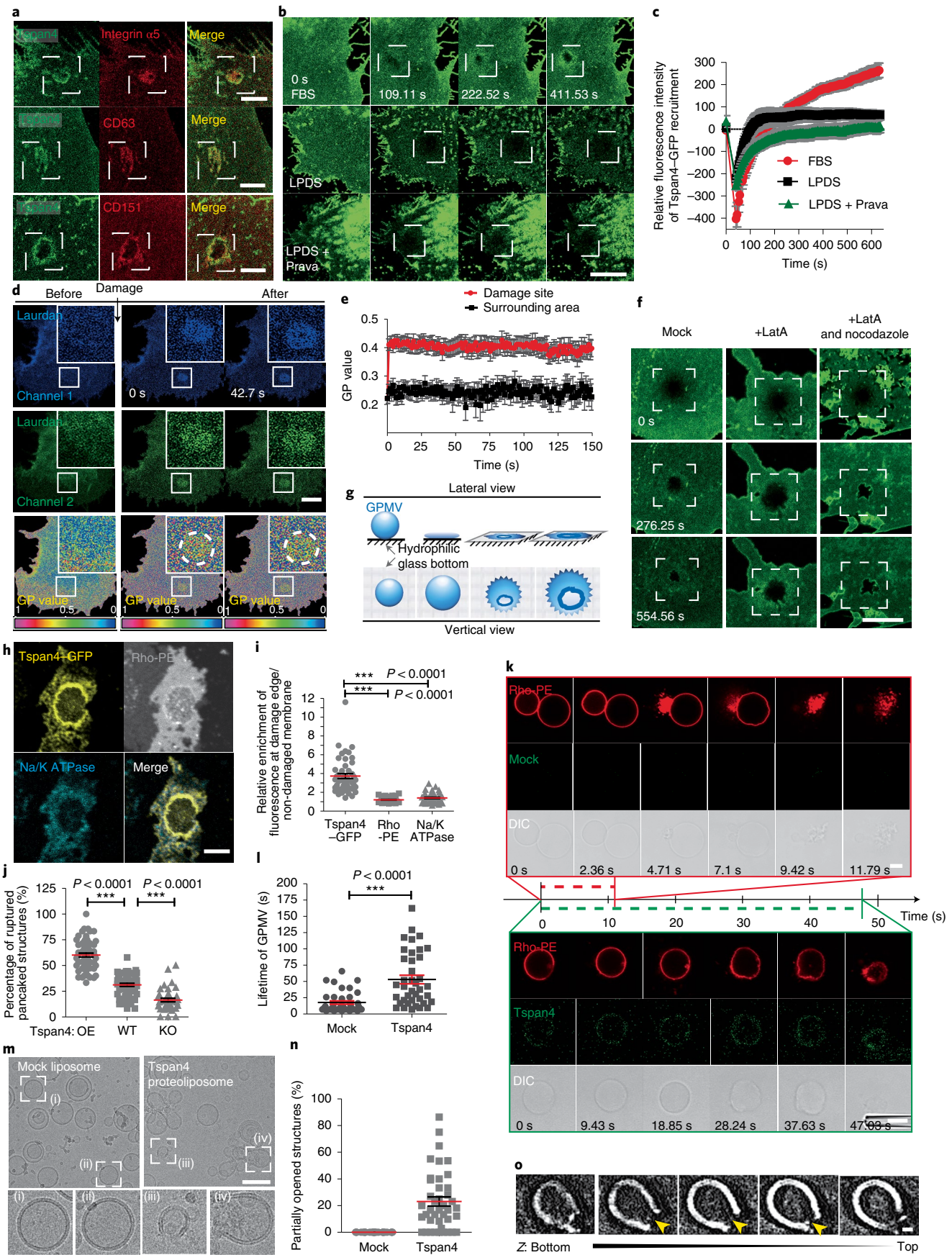
depletion blocks assembly of the TEMA ring and notably increases the influx of PI (Fig. 3b,c and Extended Data Fig. 3a–d). Together, these data suggest that Tspan4-GFP is indeed recruited to the damage site in the form of TEMs. Once the TEMs reach the damage site, they assemble into a micrometre-scale TEMA.

Membrane microdomains, like Tetraspanin-enriched domains, tend to be in a liquid-ordered phase because of their high cholesterol concentration, which results in high membrane rigidity. To test whether the TEMAs assembled around the damage site is in a liquid-ordered phase, we used the phase dye laurdan. Generalized polarization of laurdan changes only with phase state; thus, laurdan has been widely used to identify phase states in membranes^{21,22}. Laurdan-dye staining revealed a ring-like structure enclosing the damage site with a generalized-polarization value of approximately 0.4; thus, the TEMAs enclosing the damage site is in the liquid-ordered phase (Fig. 3d,e).

Next, we investigated the source of the TEMs. Tspan4-GFP is localized on the plasma membrane and on intracellular vesicles. The fact that recruitment of Tspan4 is not dependent on the cytoskeleton (Fig. 3f) suggests that Tspan4 is probably recruited from the plasma membrane.

We hypothesized that physical properties, rather than complicated biological processes, underlie the mechanism of TEM-mediated membrane repair. We reasoned that the membrane repair process

Fig. 3 | Tspan4-enriched microdomains increase the resistance of membranes. **a**, Confocal microscopy images of Integrin α5- (top), CD63- (middle) and CD151-mCherry (bottom) in photodamaged Tspan4-GFP NRK cells. White dashed boxes, damage areas. **b**, Tspan4-GFP-expressing NRK cells pre-treated with 10% full cholesterol medium (fetal bovine serum, FBS; top), cholesterol depletion medium (lipoprotein-deficient serum, LPDS; middle) or LPDS with 30 μM pravastatin (bottom) were observed before and after photodamage using confocal microscopy. White dashed boxes, damage areas. **c**, Levels of Tspan4-GFP recruitment to the damage site in **b**. Data are the mean ± s.e.m. of $n=19$ (FBS), 20 (LPDS) and 22 (LPDS + pravastatin) cells. **d**, Intensity images (top and middle) and the corresponding generalized polarization images (bottom) before and after photodamage of laurdan-labelled NRK cells expressing Tspan4-mCherry. Imaging was performed by two-photon fluorescence microscopy. Insets: magnified views of the regions in the white boxes (3 times magnification). Dashed circle, the site of Tspan4-enriched ring. **e**, Generalized-polarization (GP) values over time at the damage site and the surrounding area. Data are the mean ± s.e.m. of $n=17$ cells. **f**, Time-lapse images after photodamage of Tspan4-GFP-expressing NRK cells that were mock treated, or exposed to latrunculin A (500 nM) or latrunculin A (500 nM) + nocodazole (10 μM). White dashed boxes, damage areas. **g**, Schematic of the in vitro collapse assay. **h**, Immunofluorescence images of Tspan4-GFP GPMVs in the in vitro collapse assay in **g**. **i**, Levels of fluorescence enrichment at the edge of the damaged membrane relative to the undamaged membrane as described in Extended Data Fig. 4b. Data are the mean ± s.e.m. of $n=48$ GPMVs. **j**, Percentage of ruptured pancake membrane structures in NRK cells per random view. Data are the mean ± s.e.m. of $n=61$ (Tspan4-overexpressing, OE), 57 (WT) and 40 (Tspan4-KO, KO) random views. **k**, Time-lapse images of GPMVs with (bottom) or without (top) Tspan4-GFP treated with detergent using a micropipette system. DIC, differential interference contrast. **l**, Scale bars, 5 μm. **m**, Lifetime of detergent-treated GPMVs with or without Tspan4-GFP. Data are the mean ± s.e.m. of $n=39$ GPMVs for each group. **n**, Cryogenic electron microscopy images of proteoliposomes with (right) or without (left) embedded Tspan4 after routine cryo-EM sample preparation. Magnified views of the regions in the white boxes are shown (bottom) (2.6 times magnification). Scale bar, 100 nm. **o**, Percentage of partially opened structures per random view. Data are the mean ± s.e.m. of $n=34$ (mock liposome) and 41 (Tspan4 proteoliposome) random views. **p**, Reconstructed cryo-electron tomographic Z-stack images of partially opened structures in Tspan4 proteoliposomes. Yellow arrows, partially opened site. **q**, Scale bars, 10 μm. **r**, The experiments were independently performed three times. **s**, Individual data points are shown. **t**, Two-tailed unpaired Student's *t*-tests were used for statistical analyses. Prava, pravastatin; and latA, latrunculin A.



could probably be reconstituted in vitro. To test this hypothesis, we generated giant plasma membrane vesicles (GPMVs) from normal rat kidney (NRK) cells with or without Tspan4–GFP expression. We then adapted the widely used protocol for generating a supported bilayer by dropping GPMVs onto a hydrophilic glass surface (Fig. 3g). When GPMVs contact the hydrophilic surface they become flatter and form a pancake-shaped double-membrane structure that becomes an increasingly thinner. As the ‘pancake’ gets larger and thinner, the upper layer of the membrane ruptures at its centre, eventually forming a single-membrane bilayer attached to the supporting surface. We observed that the membrane rupture of GPMVs derived from cells with Tspan4–GFP overexpression caused rapid recruitment of Tspan4–GFP to the edge of the rupture site; in contrast, membrane proteins such as Na/K ATPase and GFP-CAAX were not recruited to the rupture site, indicating that this process is highly specific (Fig. 3h,i and Extended Data Fig. 4a,b). Furthermore, the presence of Tspan4 stabilized the ruptured pancake structure, preventing it from collapsing into a single-membrane bilayer (Fig. 3j and Extended Data Fig. 4c). This experiment further supports our conclusion that the recruitment of Tspan4 to the membrane damage site is driven by lateral assembly of Tetraspanin-enriched microdomains at the damage site. Moreover, it indicates that the assembly of Tetraspanin-enriched microdomains can stabilize the membrane damage site.

As we showed earlier, localized delivery of detergent can cause the assembly of Tspan4–GFP rings in cells. Thus, we tested whether GPMVs from cells expressing Tspan4–GFP are more resistant to detergent. In this system GPMVs from control and Tspan4–GFP-expressing cells were generated and the membranes were visualized using rhodamine-PE (Rho-PE). We then applied detergent through a micropipette and used live imaging to monitor the process. We found that Tspan4–GFP GPMVs are much more resistant to detergent. Following exposure to 0.5% foscholine-12, the GPMVs from Tspan4-expressing cells survived substantially longer than the control GPMVs (Fig. 3k,l). Detailed live-imaging analysis showed that control GPMVs explode immediately after application of detergent by micropipette. In contrast, following exposure of Tspan4 GPMVs to detergent, the Rho-PE signal in a small section of the membrane becomes weaker, which suggests that this part of the membrane is damaged. The damaged membrane is quickly expelled from the GPMV and the damaged site closes again. This process keeps repeating, eventually resulting in a smaller but still intact GPMV (Extended Data Fig. 4d).

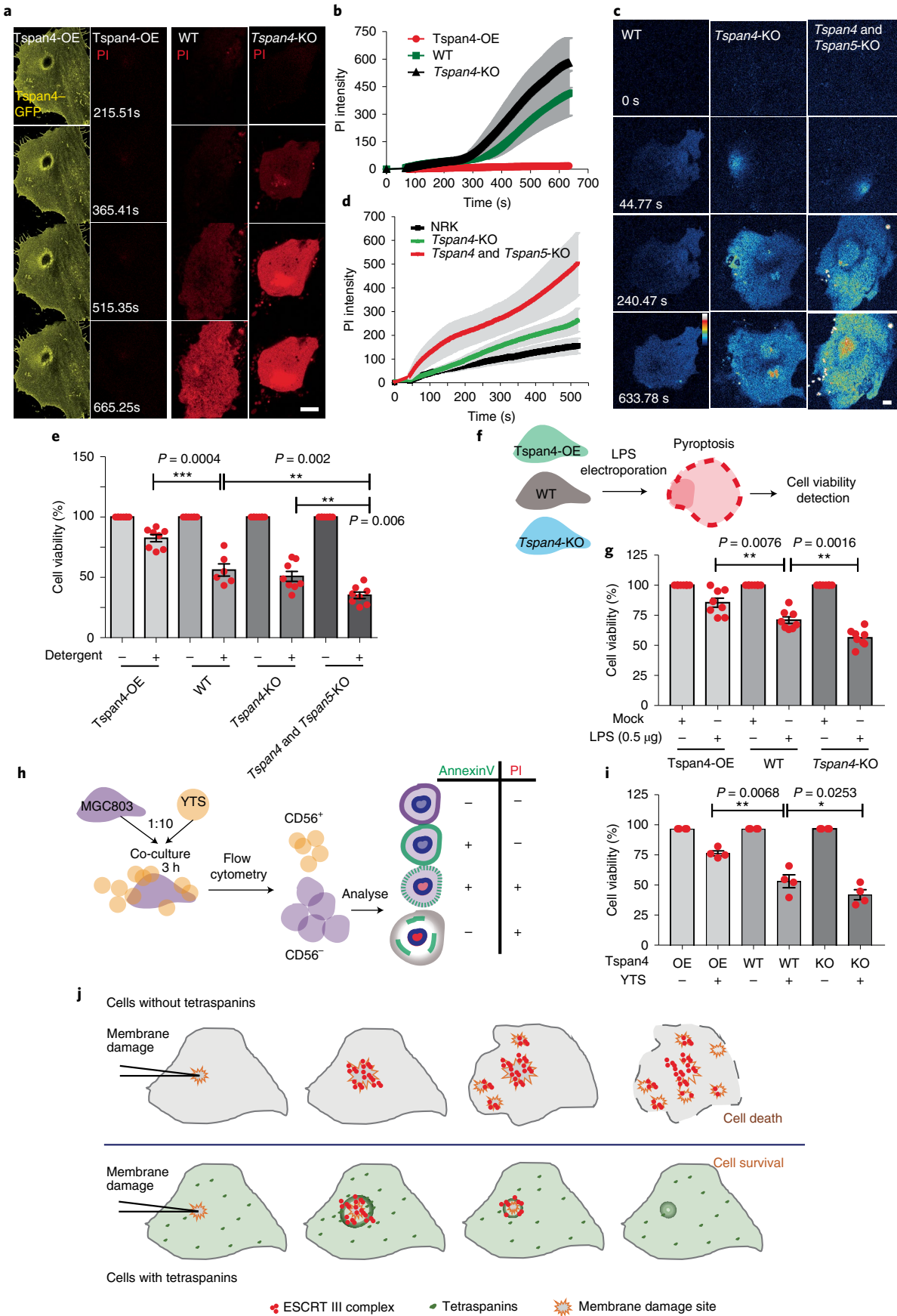
By serendipity, we found that Tspan4–GFP-embedded proteoliposomes show an unusual morphology under cryogenic electron microscopy (cryo-EM). Control liposomes, with no Tspan4, were all intact in the cryo-EM images. In contrast, using cryo-electron tomography, we observed that some of the Tspan4–GFP-embedded proteoliposomes ruptured but still retained vesicular morphology (Fig. 3m-o and Supplementary Videos 4,5). We observed dishevelled membrane fragments close to the sites of rupture, which are

probably the expelled fragments of damaged membrane. Our interpretation of this observation is that the process of cryo-EM sample preparation causes mild membrane damage, possibly by liquid-level extrusion during blotting²³. In the control liposomes, all of the damaged vesicles are quickly destroyed and thus cannot be visualized by cryo-EM. In the Tspan4–GFP-embedded proteoliposomes, the intermediate ‘open’ stage of vesicle rupture is stabilized by Tspan4 and subsequently frozen and preserved, permitting visualization by cryo-EM. Together, these data suggest that Tspan4 promotes membrane damage repair by maintaining structural integrity during membrane rupture and by isolating the damaged area. In this way Tspan4 prevents the catastrophic propagation of local damage into global damage.

Next, we tested whether Tspan4 can protect cells from membrane damage. Uptake of PI was used as a measure of the extent of membrane damage. We found that overexpression of Tspan4 notably reduced the uptake of PI in cells undergoing photodamage (Fig. 4a,b) or detergent-induced membrane damage (Extended Data Fig. 5a,b), whereas *Tspan4*-KO had a relatively minor effect on enhancing PI entry. This suggests that Tspan4 plays a role in protecting cells from photodamage- and detergent-induced cell death. There are 33 Tetraspanins in mammalian cells. RNA sequencing indicated that *Tspan5*, -7, -3 and -31 (in addition to *Tspan4*) have relatively high expression levels in NRK cells, which raises the possibility that functional redundancy of Tetraspanins may explain the minor effect of *Tspan4*-KO. To test this possibility, we constructed double-KO cell lines—that is, *Tspan4* and *Tspan5*, *Tspan4* and *Tspan7*, *Tspan4* and *Tspan3*, and *Tspan4* and *Tspan31*. The *Tspan4* and *Tspan5* double-KO cells showed notably increased PI entry. Similarly, when we labelled the damaged membrane using the lipophilic dye FM 1-43, the *Tspan4* and *Tspan5* double-KO cells had a higher FM 1-43 signal, indicating that there was more damaged membrane on these cells. Moreover, the *Tspan4* and *Tspan5* double-KO cells showed a marked enhancement of detergent-induced viability loss (Fig. 4c-e and Extended Data Fig. 5c-e). These results suggest that redundancy between Tspan4 and Tspan5 may explain the minor effect of *Tspan4*-KO.

Finally, we tested the physiological relevance of Tspan4-enhanced membrane repair. Physiological stimuli such as pyroptosis have been shown to cause massive membrane damage, which can be countered by the ESCRT-mediated membrane repair mechanism. We found that Tspan4–GFP overexpression protected cells from pyroptosis induced by lipopolysaccharide (LPS) transfection²⁴ (Fig. 4f). Conversely, *Tspan4*-KO sensitized cells to LPS transfection-induced pyroptosis, and simultaneous KO of *Tspan5* and *Tspan4* further exacerbated this sensitivity (Fig. 4g and Extended Data Fig. 5f). These results suggest that Tetraspanin-mediated membrane repair plays an important role in maintaining cell viability during pyroptosis. Natural killer (NK) cells kill their target cells by perforin-mediated membrane disruption and apoptosis²⁵⁻³¹. As described earlier, we observed the recruitment of blue fluorescent protein (BFP)-labelled

Fig. 4 | Tspan4 increases cell viability following membrane damage. **a**, Images of Tspan4-overexpressing, WT and *Tspan4*-KO NRK cells after photodamage. PI influx was used to indicate cell death. Scale bar, 10 µm. **b**, PI intensity of cells in **a** after photodamage. Data are the mean ± s.e.m. of $n=23$ cells for each group from three independent experiments. **c**, Heatmap images of PI entry signals in WT, *Tspan4*-KO and *Tspan4* and *Tspan5* double-KO NRK cells after photodamage treatment. Time-lapse imaging was conducted using confocal microscopy. Scale bar, 5 µm. The colour legend from dark to white indicates the increasing fluorescent intensity. **d**, PI intensity of the cells in **c** after photodamage. Data are the mean ± s.e.m. of $n=21$ (WT), 16 (*Tspan4*-KO) and 30 (*Tspan4* and *Tspan5* double-KO) NRK cells from four independent experiments. **e**, Cell viability of each group of NRK cells following detergent treatment. Data are the mean ± s.e.m. of $n=6$ (WT) and 8 (all other groups) independent experiments. **f**, Schematic of the experiment to assess the effect of Tspan4 on cell viability after LPS electroporation. **g**, Cell viability for each group in **f** after PBS (mock) or LPS electroporation treatment. Data are the mean ± s.e.m. of $n=8$ independent experiments for each group. **h**, Diagram of the NK killing assay. NK cells (YTS) were co-incubated with cancer cells (MGC803); the MGC803 cells were then sorted out and analysed for viability. **i**, Viability of Tspan4-OE, WT and *Tspan4*-KO cells in the NK cell killing assay in **h**. Data are the mean ± s.e.m. of $n=4$ independent experiments for each group. **j**, Model illustrating the function of Tspan4 in the repair of membrane damage. **a,c**, The experiments were independently performed three (**a**) and four (**c**) times with similar results; representative images are shown. **e,g,i**, Two-tailed unpaired Student’s t-tests were used for statistical analyses; individual data points are shown. OE, overexpression.



Tspan4 to the contact sites between NK cells and their target cells (Fig. 1e). Therefore, we also tested whether Tspan4 protects target cells from NK cells. We found that overexpression of Tspan4 indeed protects target cells from NK-mediated killing, whereas *Tspan4*-KO sensitizes target cells to NK-mediated cell death. Thus, Tspan4 protects target cells from NK cells (Fig. 4h,i and Extended Data Fig. 6).

In conclusion, we propose that Tspan4 plays an important role in membrane repair by mediating assembly of a TEM, which seals off the damage site to prevent it from expanding and thus facilitates membrane repair (Fig. 4j). This mechanism, which could be viewed as a parallel and possibly indirect mechanism, maintains membrane integrity following damage in synergy with the ESCRT machinery and possibly other mechanisms that directly repair wounds smaller than 100 nm. It is worth noting that TEMs are known for their ability to recruit a large array of membrane proteins. Therefore, it is highly plausible that TEMs can also promote membrane repair by recruiting other repair machinery factors. Moreover, given the kinetics of Tspan4 recruitment, this mechanism may also contribute to post-repair remodelling.

Online content

Any methods, additional references, Nature Research reporting summaries, source data, extended data, supplementary information, acknowledgements, peer review information; details of author contributions and competing interests; and statements of data and code availability are available at <https://doi.org/10.1038/s41556-022-00920-0>.

Received: 20 February 2021; Accepted: 22 April 2022;

Published online: 2 June 2022

References

- McNeil, P. L. & Terasaki, M. Coping with the inevitable: how cells repair a torn surface membrane. *Nat. Cell Biol.* **3**, E124–E129 (2001).
- Andrews, N. W., Almeida, P. E. & Corrotte, M. Damage control: cellular mechanisms of plasma membrane repair. *Trends Cell Biol.* **24**, 734–742 (2014).
- Jimenez, A. J. & Perez, F. Physico-chemical and biological considerations for membrane wound evolution and repair in animal cells. *Semin. Cell Dev. Biol.* **45**, 2–9 (2015).
- Davenport, N. R., Sonnemann, K. J., Eliceiri, K. W. & Bement, W. M. Membrane dynamics during cellular wound repair. *Mol. Biol. Cell* **27**, 2272–2285 (2016).
- Christ, L., Raiborg, C., Wenzel, E. M., Campsteijn, C. & Stenmark, H. Cellular functions and molecular mechanisms of the ESCRT membrane-scission machinery. *Trends Biochem. Sci.* **42**, 42–56 (2017).
- Horn, A. & Jaiswal, J. K. Cellular mechanisms and signals that coordinate plasma membrane repair. *Cell. Mol. Life Sci.* **75**, 3751–3770 (2018).
- Radulovic, M. & Stenmark, H. ESCRTs in membrane sealing. *Biochem. Soc. Trans.* **46**, 773–778 (2018).
- Meng, X. et al. Actin polymerization and ESCRT trigger recruitment of the fusogens syntaxin-2 and EFF-1 to promote membrane repair in *C. elegans*. *Dev. Cell* **54**, 624–638 (2020).
- Jimenez, A. J. et al. ESCRT machinery is required for plasma membrane repair. *Science* **343**, 1247136 (2014).
- Ruhl, S. et al. ESCRT-dependent membrane repair negatively regulates pyroptosis downstream of GSDMD activation. *Science* **362**, 956–960 (2018).
- Gong, Y. N. et al. ESCRT-III acts downstream of MLKL to regulate necrotic cell death and its consequences. *Cell* **169**, 286–300 (2017).
- Beckwith, K. S. et al. Plasma membrane damage causes NLRP3 activation and pyroptosis during Mycobacterium tuberculosis infection. *Nat. Commun.* **11**, 2270 (2020).
- Charrin, S. et al. Lateral organization of membrane proteins: tetraspanins spin their web. *Biochem. J.* **420**, 133–154 (2009).
- Le Naour, F., Andre, M., Boucheix, C. & Rubinstein, E. Membrane microdomains and proteomics: lessons from tetraspanin microdomains and comparison with lipid rafts. *Proteomics* **6**, 6447–6454 (2006).
- Hemler, M. E. Tetraspanin proteins mediate cellular penetration, invasion, and fusion events and define a novel type of membrane microdomain. *Annu. Rev. Cell Dev. Biol.* **19**, 397–422 (2003).
- Zuidzherwoude, M. et al. The tetraspanin web revisited by super-resolution microscopy. *Sci. Rep.* **5**, 12201 (2015).
- Wrigley, J. D., Ahmed, T., Nevett, C. L. & Findlay, J. B. Peripherin/rds influences membrane vesicle morphology. Implications for retinopathies. *J. Biol. Chem.* **275**, 13191–13194 (2000).
- Runge, K. E. et al. Oocyte CD9 is enriched on the microvillar membrane and required for normal microvillar shape and distribution. *Dev. Biol.* **304**, 317–325 (2007).
- Miyado, K. et al. The fusing ability of sperm is bestowed by CD9-containing vesicles released from eggs in mice. *Proc. Natl Acad. Sci. USA* **105**, 12921–12926 (2008).
- Huang, Y. et al. Migrasome formation is mediated by assembly of micron-scale tetraspanin macromolecules. *Nat. Cell Biol.* **21**, 991–1002 (2019).
- Parasassi, T., Gratton, E., Yu, W. M., Wilson, P. & Levi, M. Two-photon fluorescence microscopy of laurdan generalized polarization domains in model and natural membranes. *Biophys. J.* **72**, 2413–2429 (1997).
- Gaus, K., Zech, T. & Harder, T. Visualizing membrane microdomains by laurdan 2-photon microscopy. *Mol. Membr. Biol.* **23**, 41–48 (2006).
- Noble, A. J. et al. Routine single particle CryoEM sample and grid characterization by tomography. *eLife* **7**, e34257 (2018).
- Wang, D. et al. Magnesium protects against sepsis by blocking gasdermin D N-terminal-induced pyroptosis. *Cell Death Differ.* **27**, 466–481 (2020).
- Trapani, J. A. & Smyth, M. J. Functional significance of the perforin/granzyme cell death pathway. *Nat. Rev. Immunol.* **2**, 735–747 (2002).
- Zhang, Z. B. et al. Gasdermin E suppresses tumour growth by activating anti-tumour immunity. *Nature* **579**, 415 (2020).
- Zhou, Z. W. et al. Granzyme A from cytotoxic lymphocytes cleaves GSDMB to trigger pyroptosis in target cells. *Science* **368**, eaaz7548 (2020).
- Russell, J. H. & Ley, T. J. Lymphocyte-mediated cytotoxicity. *Annu. Rev. Immunol.* **20**, 323–370 (2002).
- de Saint Basile, G., Menasche, G. & Fischer, A. Molecular mechanisms of biogenesis and exocytosis of cytotoxic granules. *Nat. Rev. Immunol.* **10**, 568–579 (2010).
- Kumar, S. Natural killer cell cytotoxicity and its regulation by inhibitory receptors. *Immunology* **154**, 383–393 (2018).
- Voskoboinik, I., Whisstock, J. C. & Trapani, J. A. Perforin and granzymes: function, dysfunction and human pathology. *Nat. Rev. Immunol.* **15**, 388–400 (2015).

Publisher's note Springer Nature remains neutral with regard to jurisdictional claims in published maps and institutional affiliations.

© The Author(s), under exclusive licence to Springer Nature Limited 2022

Methods

Plasmids and cell culture. *Plasmid construction.* Complementary DNAs to genes coding Tetraspanins were cloned into pEGFP-N₁ or pmCherry-N₁ for imaging, which meant that GFP or mCherry was fused at the carboxy terminus of the *Tspan* genes. All *Tspan* genes as well as the *Chmp3*, *Chmp4b*, *Vps4a*, *Chmp7* and *Integrin a5* genes were originally cloned from the rat genome.

Cell culture. Adherent cells—that is, NRK, MGC803 and L929 cells and their derivatives—were cultured at 37 °C and 5% CO₂ in DMEM medium supplemented with 10% serum and 1% penicillin–streptomycin. For suspension cells, YTS cells were cultured at 37 °C and 5% CO₂ in RPMI 1640 medium supplemented with 10% serum and 1% penicillin–streptomycin.

Generation of KO cell lines. *Chmp4b*-KO cells. The *Chmp4b* gene in NRK cells was deleted using a modified PX458 plasmid (provided by W. Guo from Zhejiang University) that contains two single guide RNAs (sgRNAs) coupled to Cas9 nuclease. The sgRNA sequences used for CRISPR-Cas9 were 5'-GAGGATCGCG CACTGCATGC-3' (sgRNA1) and 5'-GTACCAATCAACAAACAGGAC-3' (sgRNA2). After transfection (72 h), the cells were seeded into 96-well plates by fluorescence-activated cell sorter selection of EGFP signal expression. DNA fragments containing the sgRNA-targeted region were amplified from the genomic DNA of these monoclonal cells and sequenced to pick out the correct clones. The test primer sequences were 5'-AGCCGAAAACCTCAGACT-3' (forward) and 5'-TGGATATTGTAAGCACTCTCA-3' (reverse).

Tspan4 and *Tspan5* double-KO cells. The *Tspan5* gene was deleted in previously generated *Tspan4*-KO NRK cells²⁰ following the same method described earlier. The sgRNA sequences used for CRISPR-Cas9 were 5'-GCTCAGCCGCG GACCGAG-3' (sgRNA1) and 5'-GGCAGAGCGTGGTGTCTAAAT-3' (sgRNA2). The test primer sequences were 5'-CTACCCCTGGCTCTCTAAAT-3' (forward) and 5'-TGCAAGGAGATACACGCTGA-3' (reverse).

Cell transfection. For NRK cells and their derivatives, one-third of a 6-cm dish of cells was transfected with 2 µg DNA via Amaxa nucleofection using solution T and programme X-001, and then cultured for 15 h for protein expression. For L929 and MGC803 cells, a 3.5-cm dish of cells was transfected with 4 µg DNA using a Lipofectamine 3000 transfection kit (Invitrogen) and then cultured for 15–18 h for protein expression.

Photodamage assay. Cell photodamage experiments were conducted under galvanometer scanning mode using a NIKON A1 confocal microscope fitted with a ×100 oil objective and 3× zoom. For statistical analysis of the Chmp4b-mCherry⁺ area and intensity, the imaging areas were magnified ×2. The area of interest was damaged using a laser (405 nm) with 100% output for 6–8 s per frame and 7–8 loops. Immediately after damage, the laser power was decreased to 2% and each field of 512 × 512 pixels was imaged for 10–15 min.

SIM imaging of photodamaged sites. Cells co-expressing *Tspan4*-GFP and Chmp4b-mCherry were seeded onto gridded glass-bottomed dishes for 15 h. The position of the target cell was located and the cell was photodamaged using a confocal microscope. Immediately after damage, the cell was fixed with 4% paraformaldehyde for 5 min at room temperature and washed once in PBS. The damaged cell was then imaged using SIM (Nikon N-SIM S) and reconstructed using a standard stack-reconstruction process.

Detergent treatment assay. *Micropipette glass needle.* Cells cultured on a 24-mm glass coverslip were placed on a micropipette system and the glass needle was positioned close to the target area on the cell. The cell was injected with 0.02% Triton X-100 or mock injected and time-lapse imaging was begun simultaneously.

In a cell culture chamber. Cells cultured in a 3.5-cm confocal dish were placed onto a confocal microscopy system and fixed in the x-y position depending on the chosen field. The culture medium was gently replaced by fresh culture medium with 0.013% Triton X-100 or not (as control) and time-lapse images (512 × 512 pixels) were acquired for 20 min.

Laurdan-dye staining, imaging and generalized polarization-value calculation. For GP-value calibration, 5 µM laurdan dye in dimethylsulfoxide at 22 °C was added into a confocal dish and then excited by an 800-nm laser in a two-photon microscopy system. Two images were simultaneously captured in channel 1 (400–460 nm) and channel 2 (470–530 nm).

Laurdan dye (5 µM) in fresh medium was added to the cells for 30 min for pre-staining at 37 °C. The cells were first imaged by an 800-nm laser using the two-photon microscopy mode and then quickly photodamaged in confocal microscopy mode. The damaged cells were then time-lapse imaged by two-photon microscopy for 3 min.

The generalized-polarization values were calibrated and calculated as described previously^{21,22} and presented as a statistical plot. Images from channels 1 and 2 were calibrated and analysed as before for presentation in GP-value mode.

In vitro detergent resistance assay. *Preparation of GPMVs.* Cells were cultured in 12.5-ml flasks for 15 h until they reached 90–100% confluence. After removing the culture medium, the cells were washed once in GPMV buffer (10 mM HEPES, 2 mM CaCl₂ and 150 mM NaCl, pH 7.4). A 1-ml volume of GPMV buffer containing freshly added 2 mM dithiothreitol, 25 mM formaldehyde and 10 µg ml⁻¹ Rho-PE (Avanti) was applied to the cells at 37 °C for 1 h, with shaking at 70 r.p.m. Finally, GPMVs were prepared in the 1-ml suspension.

In vitro micropipette treatment. GPMVs were placed in a micropipette system and the glass needle was set close to the target GPMV. The GPMVs were injected with 0.5% foscholine-12 or mock injected and time-lapse imaging was started simultaneously.

In vitro collapse assay. *Preparation of hydrophilic glass-bottomed chambers.* A glass-bottomed chamber for confocal imaging was glow-discharged using a plasma cleaning device (PDC-32G, Harrick Plasma) with vacuum treatment for 2.5 min and a 60-s exposure to high-level ionizing radiation. The chamber was placed on the imaging adaptor and a sample of GPMVs (3 µl) was applied to the centre of the base of the chamber. The lid was added and the chamber/samples were allowed to stand for 3 min at room temperature. Time-lapse images (512 × 512 pixels) were then acquired for 10–15 min. For statistical analysis, images were collected randomly about 20 min after the samples were applied to the chamber. For immunofluorescence staining, the suspension was wiped off 20 min after the samples were applied to the chamber, the samples were fixed with 4% paraformaldehyde for 5 min at room temperature and then subjected to the standard immunofluorescence staining process. The following commercial antibodies were used: anti-GFP (1:500 dilution; MBL, 598); anti-α1 Na/K ATPase (1:250 dilution; Abcam, ab7671); goat anti-mouse IgG cross-adsorbed secondary antibody, Alexa Fluor 633 (1:500 dilution; Invitrogen, A21052) and goat anti-rabbit IgG cross-adsorbed secondary antibody, Alexa Fluor 488 (1:500 dilution; Invitrogen, A11008).

Preparation of proteoliposomes and cryo-EM observation. *Proteoliposome preparation.* *Tspan4*-GFP protein was purified and inserted into liposomes to form proteoliposomes as described before.

Preparation of samples for cryo-EM. Quantifoil Cu grids (200/300 mesh, R2/2) were glow-discharged using a plasma cleaning device (PDC-32G, Harrick Plasma) with vacuum treatment for 2 min and 40 s exposure to medium-level ionizing radiation. A sample (4 µl) of liposomes embedded with or without *Tspan4*-GFP was applied to the grids, followed by incubation for 1 min in a Vitrobot Mark IV system (Thermo Fisher Scientific). The grids were blotted with a blotting time of 2.5–4 s and force of zero, and then plugged into liquid ethane for vitrification. The cryo-EM samples were examined using an FEI Tecnai Arctica 200 kV transmission electron microscope.

For cryo-electron tomography, the tomographic data from the vitrified specimens were collected on an FEI Titan Krios 300 kV transmission electron microscope equipped with a Cs corrector, an energy filter and a K2 Summit direct electron detector camera (Gatan). Images were acquired at a magnification of ×64,000 (pixel size of 1.77 Å at the specimen level) and −1.5 µm defocus, with a Volta phase plate inserted to generate a phase shift of approximately 0.5π. Tilt series were collected using the SerialEM software³² at intervals of 3° from −42° to 42°, with a total dose of about 85 e[−] Å^{−2}. The structures were then reconstructed in IMOD³³ and visualized in Chimera³⁴.

Treatment of cells with LPDS. LPDS was prepared from FBS by dialysis and ultracentrifugation^{35,36}. To promote cellular cholesterol depletion, *Tspan4*-GFP-expressing NRK cells were cultured in DMEM medium supplemented with 10% FBS, LPDS or LPDS with 30 µM pravastatin (TargetMol, T0672) for 60 h as described in our previous work²⁰. The photodamage assay was then conducted on cells from each group one by one. The total cellular cholesterol levels of each group were determined using the Amplex Red cholesterol assay kit (Invitrogen, A12216) according to the manufacturer's instructions.

LPS electroporation. For NRK cells and their derivatives, 3 × 10⁵ cells were transfected with PBS (mock) or 0.5 µg LPS dissolved in PBS via Amaxa nucleofection using solution T and programme X-001, and then seeded into 96-well plates at a density of 1 × 10⁴ cells per well. Cell viability was analysed 8 h after transfection using a CellTiter-Glo luminescent cell viability kit.

NK cell killing assay. YTS (1.5 × 10⁶) and MGC803 (1.5–2 × 10⁶) cells or their derivatives were co-cultured, or cultured separately as controls, in 100 µl cell medium at 37 °C and 5% CO₂ for 3 h in 1.5-ml ventilate EP tubes. The cells were gently mixed every 30 min during the 3-h period. The cells were centrifuged at 360g and then stained for CD56-APC (1:500–1:1,000 dilution; eBioscience, 17-0566-42) at 4 °C for 30 min. After one wash in PBS, the cells were stained with AnnexinV-FITC and PI for further flow cytometry analysis following the standard procedure for AnnexinV-PI cell-death detection. The related data were analysed using the CytoFlex LX 2.3 software.

Intensity analysis. Analysis of the damage site intensity in photodamage assays.

Regions of interest (ROIs) were first designated using the NIS-analysis software. The damaged area was set as ROI 1 and a randomly selected undamaged area was set as ROI 2. After tracing the ROIs frame by frame during the whole imaging period, the absolute fluorescence intensity of all ROIs was measured. The intensity of ROI 1 was calibrated by its paired ROI 2 and normalized as a percentage for presentation in plots.

Analysis of the Chmp4b⁺ area and fluorescence intensity. The area covered by Chmp4b-mCherry signals was circled by the shortest connection between the outermost Chmp4b-mCherry punctate signals. The total substrate area of the cell was manually quantified in the DIC channel image. Based on these measurements frame by frame, the percentage of the area covered by Chmp4b-mCherry signal was calculated and the total fluorescence intensity of mCherry was measured.

Analysis of total PI intensity in the detergent treatment assays. Cell outlines were drawn on DIC channel images using the surface function in the Imaris software. The outlines were traced using the tracking function. The mean PI intensities of cells were measured frame by frame and normalized as percentages for presentation in plots.

PI, BAPTA-AM and FM 1-43. To visualize the integrity of the cell membrane during imaging-based experiments, PI (Beyotime, ST511) was added to the cell culture system at a final concentration of 4 µg ml⁻¹.

BAPTA-AM (Selleck, S7534) was added to the cell culture system at a final concentration of 10 µM for 30 min at 37 °C. The cells were then subjected to the photodamage assay.

FM 1-43 (Thermo Fisher, F35355) was added to the cell culture system at a final concentration of 5 µg ml⁻¹ for 15 min at 37 °C. The cells were then subjected to the photodamage assay.

Statistics and reproducibility. All experiments were conducted independently at least three times. *P* values were calculated using a two-tailed unpaired Student's *t*-test in GraphPad Prism5 and GraphPad Prism7. Error bars indicate the mean ± s.e.m. **P* ≤ 0.05; ***P* ≤ 0.01; ****P* ≤ 0.001; and NS, not significant. Samples were randomly allocated and no data were excluded from the analyses. No statistical method was used to pre-determine the sample size. The investigators were not blinded to allocation during experiments and outcome assessment.

Reporting summary. Further information on research design is available in the Nature Research Reporting Summary linked to this article.

Data availability

All other data supporting the findings of this study are available from the corresponding author on reasonable request. Source data are provided with this paper.

References

32. Mastronarde, D. N. Automated electron microscope tomography using robust prediction of specimen movements. *J. Struct. Biol.* **152**, 36–51 (2005).
33. Kremer, J. R., Mastronarde, D. N. & McIntosh, J. R. Computer visualization of three-dimensional image data using IMOD. *J. Struct. Biol.* **116**, 71–76 (1996).
34. Pettersen, E. F. et al. UCSF Chimera—a visualization system for exploratory research and analysis. *J. Comput. Chem.* **25**, 1605–1612 (2004).
35. Renaud, J. F. et al. Normal serum and lipoprotein-deficient serum give different expressions of excitability, corresponding to different stages of differentiation, in chicken cardiac-cells in culture. *Proc. Natl Acad. Sci. USA* **79**, 7768–7772 (1982).
36. Martin, B. J. & van Golen, K. L. A comparison of cholesterol uptake and storage in inflammatory and noninflammatory breast cancer cells. *Int. J. Breast Cancer* **2012**, 412581 (2012).

Acknowledgements

We thank the Z. Dong laboratory (Tsinghua University) for the generous gift of YTS cells and the F. Shao laboratory (NIBS) for their help with the pyroptosis-related work. We thank all of the members of L.Y.'s group for their helpful discussions. This research was supported by the Ministry of Science and Technology of the People's Republic of China (grant no. 2017YFA0503404 to L.Y.) and the National Natural Science Foundation of China (grant nos 32070691 to Y.H. and 92054301 to L.Y.).

Author contributions

L.Y. and Y.H. conceived the experiments. L.Y. wrote the paper and supervised the project. Y.H. and X.Z. carried out the experiments. All authors discussed the manuscript, commented on the project and contributed to preparing the paper.

Competing interests

The authors declare no competing interests.

Additional information

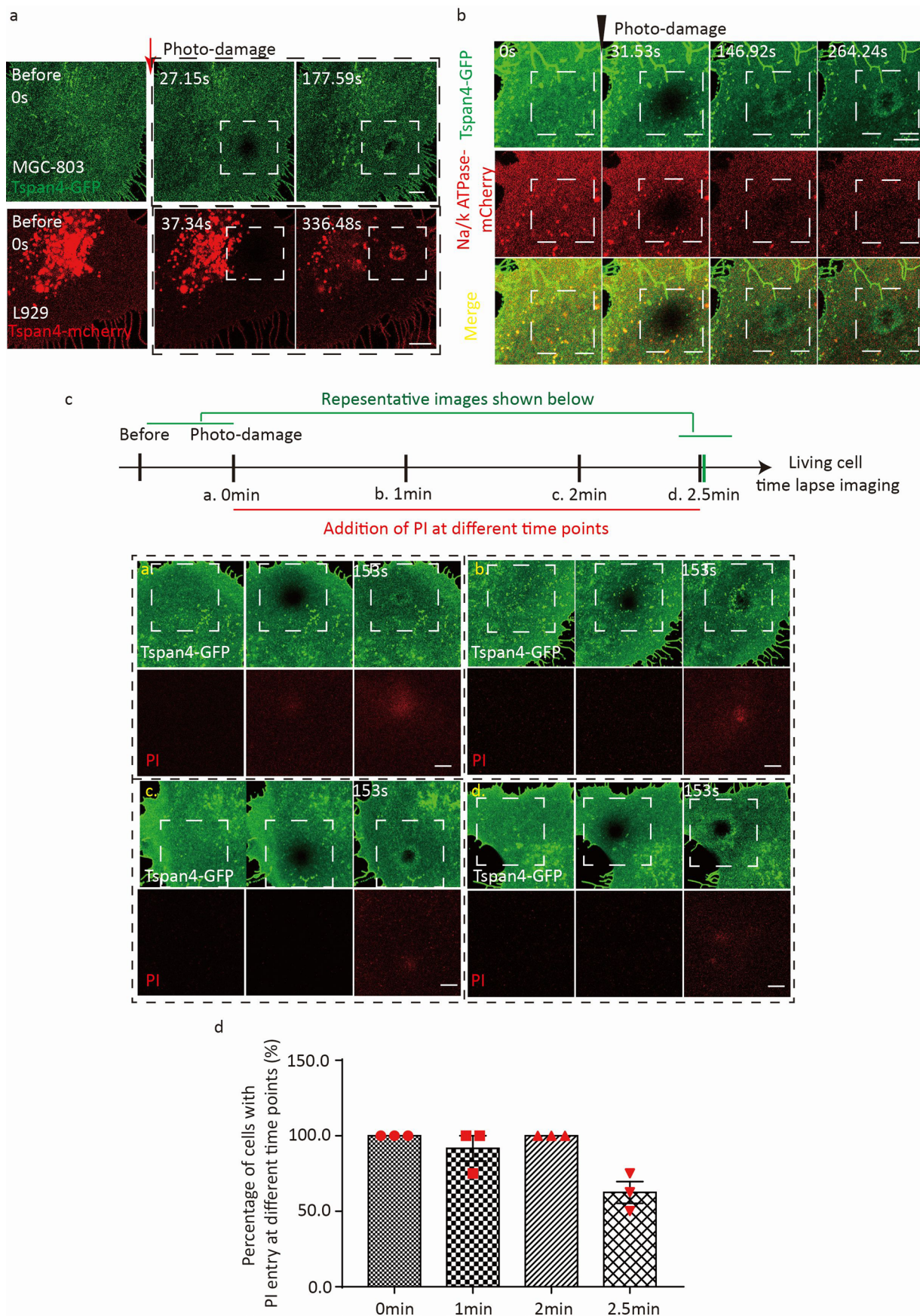
Extended data is available for this paper at <https://doi.org/10.1038/s41556-022-00920-0>.

Supplementary information The online version contains supplementary material available at <https://doi.org/10.1038/s41556-022-00920-0>.

Correspondence and requests for materials should be addressed to Li Yu.

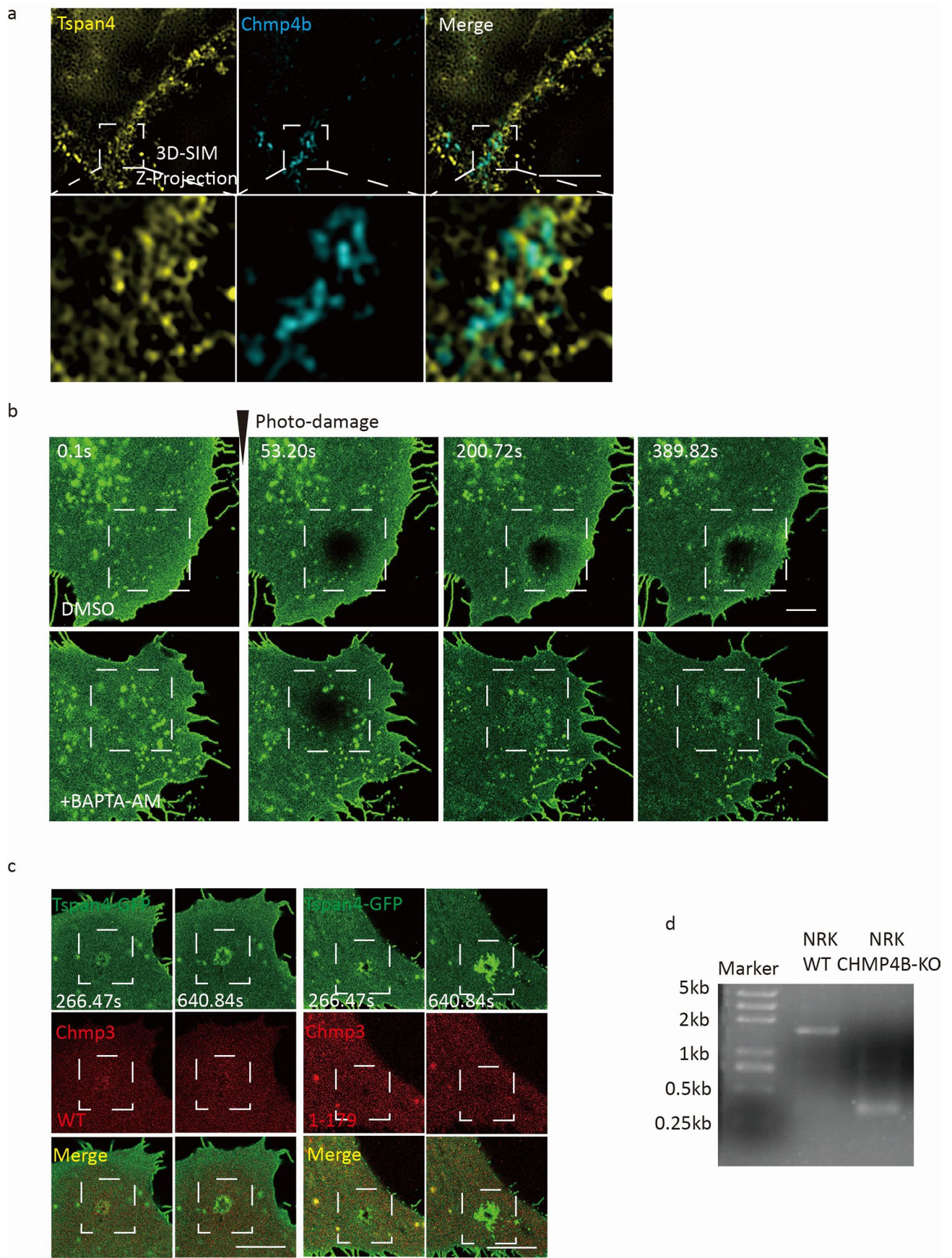
Peer review information *Nature Cell Biology* thanks Harald Stenmark, Martin Hemler and the other, anonymous, reviewer(s) for their contribution to the peer review of this work.

Reprints and permissions information is available at www.nature.com/reprints.



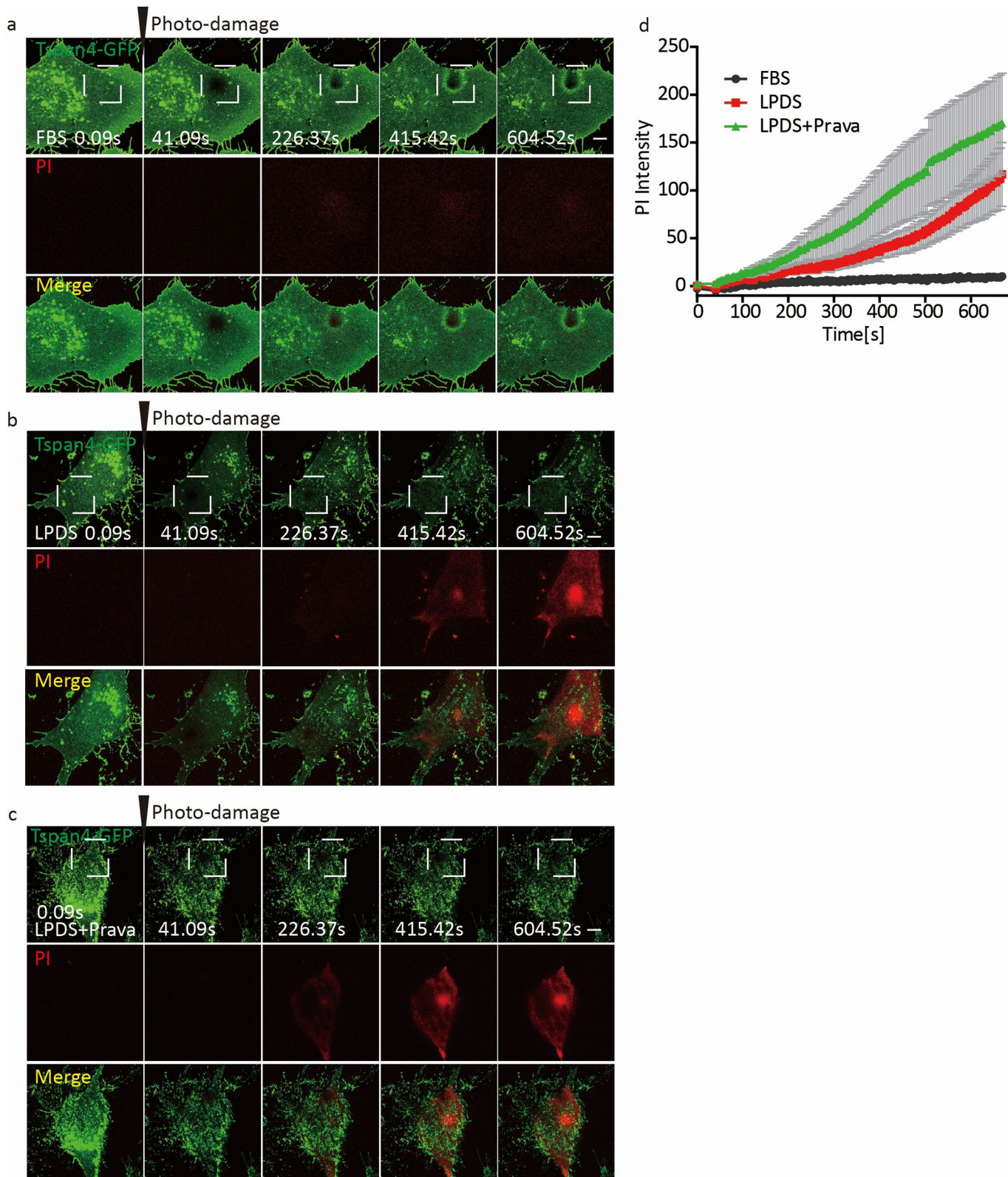
Extended Data Fig. 1 | See next page for caption.

Extended Data Fig. 1 | Tspan4 proteins are highly recruited to sites of cellular membrane damage. **a** L929 Tspan4-mCherry and MGC803 Tspan4-GFP cells were subjected to photodamage treatment and Tspan4 distribution at the damage site was observed by confocal microscopy. Scale bar, 5 μm. **b** NRK cells co-expressing Tspan4-GFP and Na/K ATPase-mCherry were photodamaged, then time-lapse images were collected by confocal microscopy. Scale bar, 5 μm. **c** After cells were photodamaged, PI was added into the system at different time points (0, 1, 2 and 2.5 min) and the PI intensity was traced. Representative images are showed. Green, Tspan4-GFP; red, PI. Scale bar, 5 μm. **d** Statistical analysis of the percentage of cells with PI entry at each time point was conducted. Mean±s.e.m., n=12 cells for the 0 min group, n=22 for the 1 min group, n=24 cells for the 2 min group and n=50 cells for the 2.5 min group from 3 independent experiments. Experiments were independently performed 3 times (a-c), and representative images are shown.

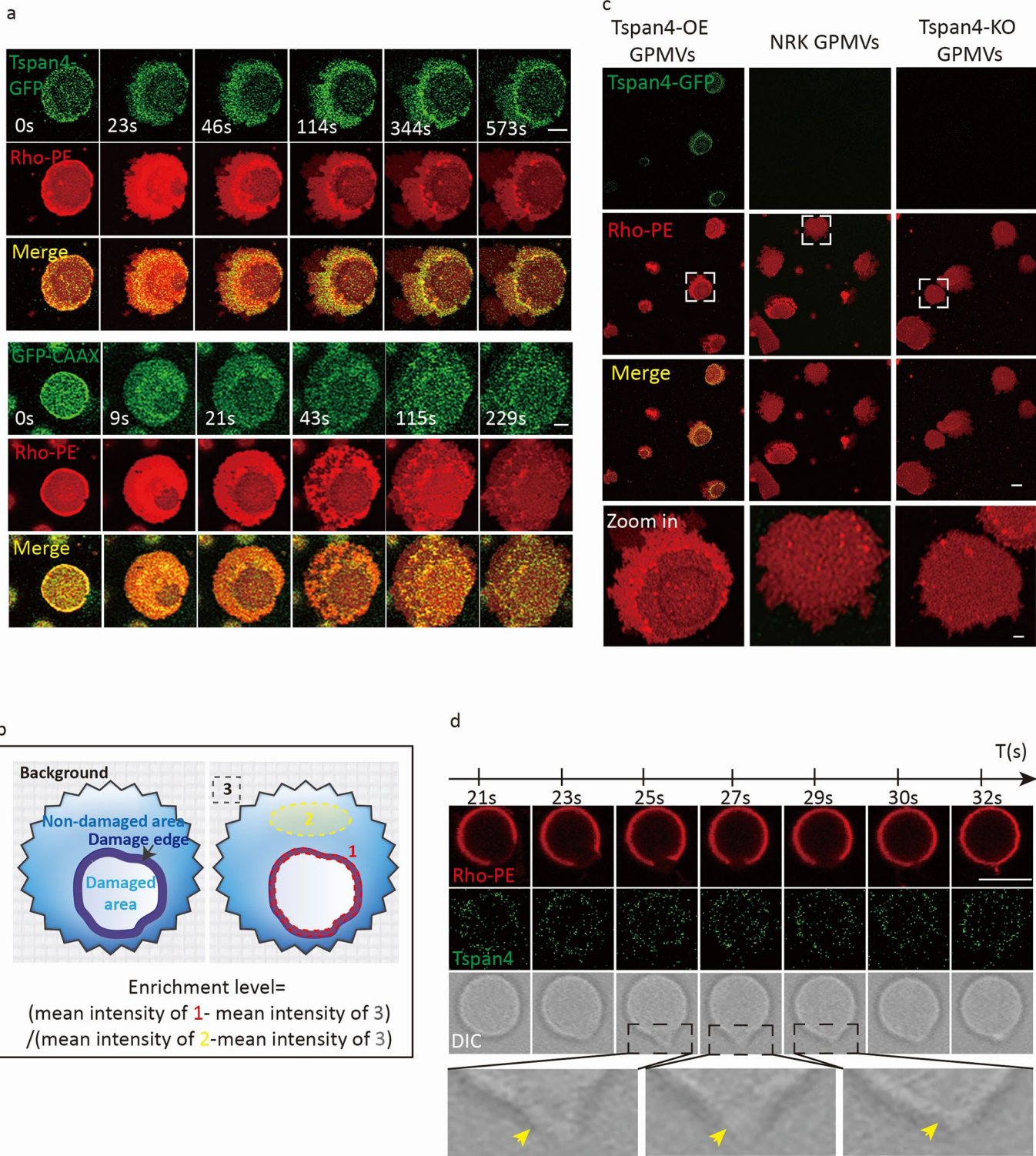


Extended Data Fig. 2 | See next page for caption.

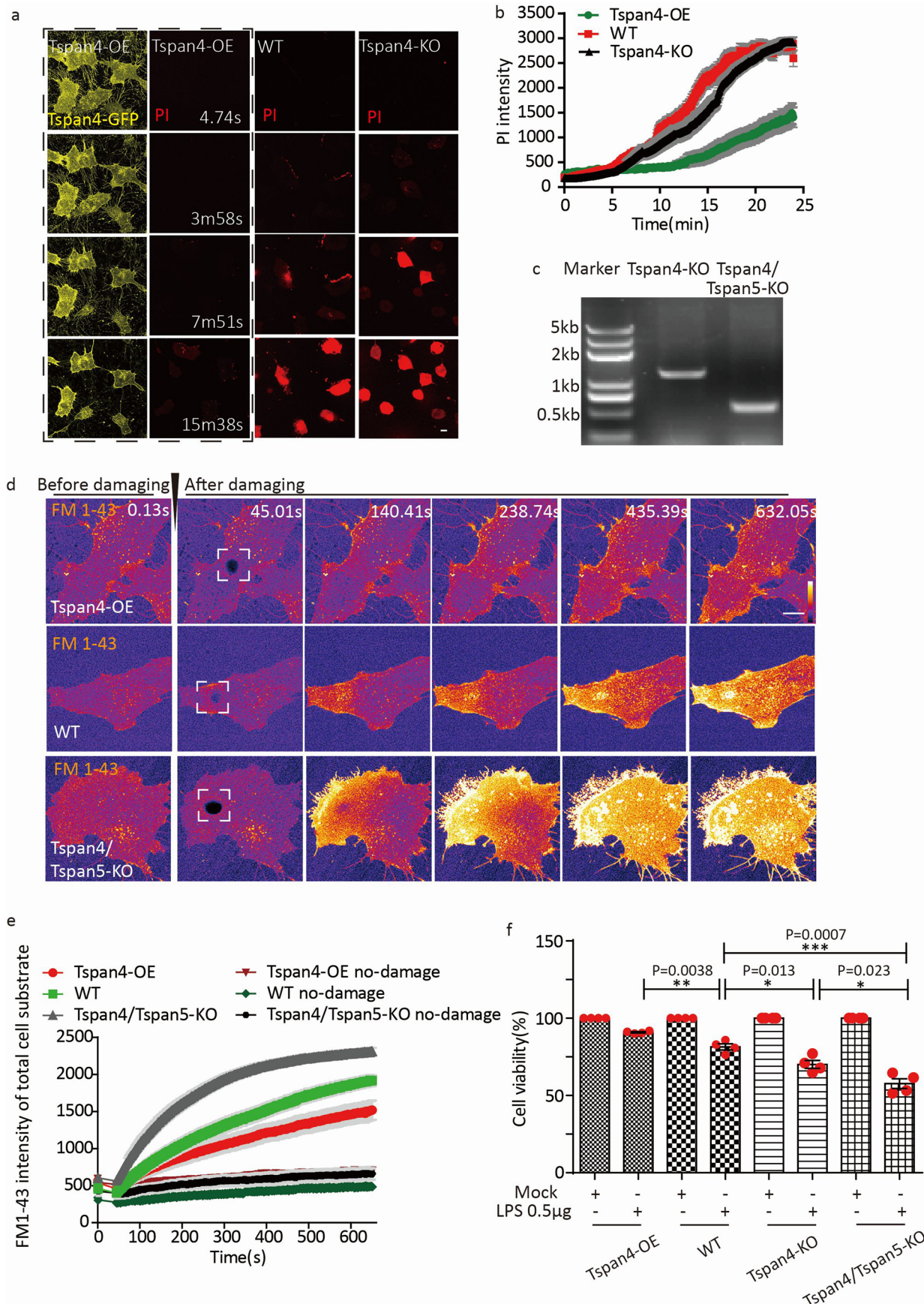
Extended Data Fig. 2 | ESCRT III activity is not required for recruitment of Tspan4 to damage sites. **a** NRK cells co-expressing Tspan4-GFP and Chmp4b-mCherry were subjected to detergent (25 μM digitonin) treatment. Z-projection images were collected by 3D-SIM. Yellow, Tspan4; cyan, Chmp4b-mCherry. Scale bar, 5 μm. **b** Tspan4-GFP overexpressing cells treated with DMSO (as control) or 10 μM BAPTA-AM were subjected to photodamage. Time-lapse images were collected by confocal microscopy. Scale bar, 5 μm. **c** Localization of Tspan4 and Chmp3 at the damage site was analysed by confocal microscopy after photodamage in cells co-expressing Tspan4-GFP and Chmp3-mCherry or Chmp3 1-179-mCherry. Scale bar, 10 μm. **d** Verification of the NRK Chmp4b knockout cell line by PCR. Experiments were independently performed 3 times (**a-d**), and representative images are shown.



Extended Data Fig. 3 | Cholesterol depletion increases the PI influx of cells after photodamage treatment. **a-c.** Tspan4-GFP NRK cells under different cholesterol depletion conditions, including 10% full cholesterol medium (FBS), cholesterol depletion medium (LPDS) and cholesterol depletion medium with 30 μ M Pravastatin, were observed by confocal microscopy before and after photodamage. PI influx was used to indicate cell death. Scale bar, 5 μ m. Experiments were performed 3 times, and representative images are shown. **d.** Statistical analysis of the PI intensity of cells under different cholesterol depletion conditions before and after photodamage treatment. Mean \pm s.e.m., n=17 cells for FBS, 15 cells for LPDS and 15 cells for LPDS + Prava from 3 independent experiments.

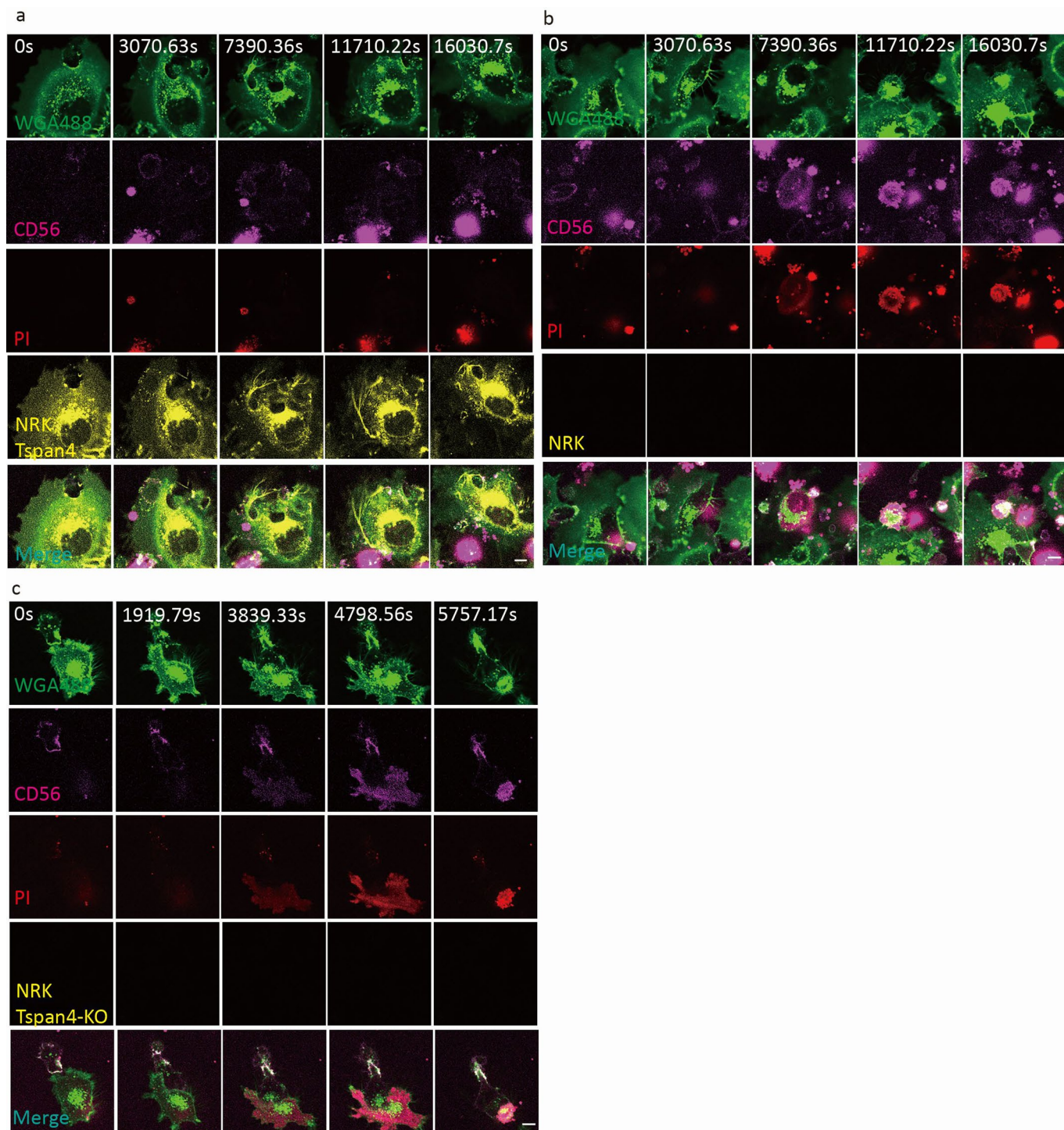


Extended Data Fig. 4 | Tspan4 proteins restrict damage expansion in vitro. **a** Time-lapse images of Tspan4-GFP GPMVs or GFP-CAAX (as control) GPMVs in the in vitro collapse assay. Green, GFP; red, Rho-PE; yellow, merge. Scale bar, 5 μ m. **b** Diagram of the method used to measure fluorescence enrichment. **c** Images were collected by confocal microscopy after Tspan4-OE GPMVs, NRK GPMVs and NRK Tspan4-KO GPMVs were used in the in vitro collapse assay. Scale bar, 10 μ m; zoom in, 2 μ m. **d** Time-lapse imaging of rupture events in Tspan4-GFP GPMVs after detergent treatment. Yellow arrow, rupture site. Scale bar, 5 μ m. Experiments were independently performed 3 times (**a** and **c-d**), and representative images are shown.



Extended Data Fig. 5 | See next page for caption.

Extended Data Fig. 5 | Tspan4 and Tspan5 enhance cell survival following membrane damage. **a** Cell death was analysed by PI permeability in NRK Tspan4-OE, NRK WT and NRK Tspan4-KO cells after detergent treatment. Cells were imaged by confocal microscopy. Scale bar, 10 μ m. **b** Statistical analysis of absolute PI intensity in NRK Tspan4-OE, NRK WT and NRK Tspan4-KO cells after detergent treatment. Mean \pm s.e.m., n=29 cells for Tspan4-OE, 42 cells for WT and 33 cells for Tspan4-KO from 3 independent experiments. **c** Verification of the Tspan4-KO Tspan5 knockout cell line by PCR. **d** Tspan4-OE (Tspan4-overexpression), WT, and Tspan4/Tspan5-KO cells pre-stained by FM 1-43 (5 μ M) were subjected to photodamage treatment and the FM 1-43 signal was monitored. Time-lapse images were collected by confocal microscopy and displayed as heatmap images. Scale bar, 10 μ m. **e** Statistical analysis of FM 1-43 fluorescence intensity of the total cell substrate during and after photodamage treatment. Mean \pm s.e.m. n=19 cells for Tspan4-OE, 30 cells for WT, 32 cells for Tspan4/Tspan5-KO, 17 cells for Tspan4-OE no-damage, 21 cells for WT no-damage and 9 cells for Tspan4/Tspan5-KO no-damage from 3 independent experiments. Statistical analysis of cell viability in each group (NRK Tspan4-OE, NRK WT, NRK Tspan4-KO, NRK Tspan4/Tspan5 double-knockout cells) after PBS or LPS electroporation treatment. Mean \pm s.e.m., n=4 independent experiments. Unpaired t-test was used.



Extended Data Fig. 6 | Tspan4 protects cancer cells from killing by NK cells. Killing of MGC803 Tspan4-BFP cells (**a**), MGC803 WT cells (**b**), or MGC803 Tspan4-KO cells (**c**) by YTS NK cells was observed by confocal microscopy. Cell death was indicated by PI influx. Yellow, BFP; cyan, CD56-APC; red, PI. Scale bar, 10 μ m. Experiments were performed 5 times (**a-c**), and representative images are shown.

Reporting Summary

Nature Research wishes to improve the reproducibility of the work that we publish. This form provides structure for consistency and transparency in reporting. For further information on Nature Research policies, see our [Editorial Policies](#) and the [Editorial Policy Checklist](#).

Statistics

For all statistical analyses, confirm that the following items are present in the figure legend, table legend, main text, or Methods section.

n/a Confirmed

- The exact sample size (n) for each experimental group/condition, given as a discrete number and unit of measurement
- A statement on whether measurements were taken from distinct samples or whether the same sample was measured repeatedly
- The statistical test(s) used AND whether they are one- or two-sided
 - Only common tests should be described solely by name; describe more complex techniques in the Methods section.*
- A description of all covariates tested
- A description of any assumptions or corrections, such as tests of normality and adjustment for multiple comparisons
- A full description of the statistical parameters including central tendency (e.g. means) or other basic estimates (e.g. regression coefficient) AND variation (e.g. standard deviation) or associated estimates of uncertainty (e.g. confidence intervals)
- For null hypothesis testing, the test statistic (e.g. F , t , r) with confidence intervals, effect sizes, degrees of freedom and P value noted
 - Give P values as exact values whenever suitable.*
- For Bayesian analysis, information on the choice of priors and Markov chain Monte Carlo settings
- For hierarchical and complex designs, identification of the appropriate level for tests and full reporting of outcomes
- Estimates of effect sizes (e.g. Cohen's d , Pearson's r), indicating how they were calculated

Our web collection on [statistics for biologists](#) contains articles on many of the points above.

Software and code

Policy information about [availability of computer code](#)

Data collection

Images about in vitro assays were collected by FV1200 and FV1000 (Olympus), living cell movies were conducted by Nikon A1 confocal microscopy (Nikon). Images and movies about Laurdan dye staining were conducted by Nikon Two-photon microscopy, Cryo-EM samples were examined with an FEI Tecnai Arctica 200 kV TEM, the tomographic data of vitrified specimen was collected on an FEI Titan Krios 300 kv TEM equipped with a Cs corrector, Tilt serials were collected by using SerialEM software and the structures were reconstructed in IMOD. Flow cytometry data were conducted by Beckman CytoFlex LX.

Data analysis

GraphPad Prism 5 and GraphPad Prism 7 were used for statistic analysis.
NIS-elements-AR4.30.02 was used for fluorescent intensity and area analysis in movies.
Flow cytometry data were analyzed by CytoFlex LX 2.3 software.
Imaris 9.0.6 was used to analyze results from PI intensitiy indetergent treatment assays.

For manuscripts utilizing custom algorithms or software that are central to the research but not yet described in published literature, software must be made available to editors and reviewers. We strongly encourage code deposition in a community repository (e.g. GitHub). See the Nature Research [guidelines for submitting code & software](#) for further information.

Data

Policy information about [availability of data](#)

All manuscripts must include a [data availability statement](#). This statement should provide the following information, where applicable:

- Accession codes, unique identifiers, or web links for publicly available datasets
- A list of figures that have associated raw data
- A description of any restrictions on data availability

Statistical data for Fig.1-Fig.4, Extended Data Fig.1, Extended Data Fig.3, and Extended Data Fig.5 have been provided as Source Data.

All other data that support the findings of this study are available from the corresponding author upon request.

Field-specific reporting

Please select the one below that is the best fit for your research. If you are not sure, read the appropriate sections before making your selection.

Life sciences Behavioural & social sciences Ecological, evolutionary & environmental sciences

For a reference copy of the document with all sections, see nature.com/documents/nr-reporting-summary-flat.pdf

Life sciences study design

All studies must disclose on these points even when the disclosure is negative.

Sample size	No statistical methods were used to determine sample size. For all the experiments, we followed the routine practice in the similar studying fields (For example, the work from A. J. Jimenez et al., <i>Science</i> , 2014). And it has been our routine practice to conduct experiments upon a relatively large but reasonable size.
Data exclusions	No data were excluded from the analysis.
Replication	For all experiments involved in this study, at least 3 times independent experiments were conducted. And the attempts at replication were successful. Detail information was involved in each figure legends and Methods, as well as statistics source data.
Randomization	All the samples were collected randomly, especially, the microscopic images were acquired randomly.
Blinding	The investigators were not blinded to allocation during experiments and outcome assessment. Within each experiment, at least one negative control group was set to ensure that only one variate was tested. And because all the data were conducted based on random sampling and reasonably large sample size, blinding is not relevant to this study.

Reporting for specific materials, systems and methods

We require information from authors about some types of materials, experimental systems and methods used in many studies. Here, indicate whether each material, system or method listed is relevant to your study. If you are not sure if a list item applies to your research, read the appropriate section before selecting a response.

Materials & experimental systems

n/a	Involved in the study
<input type="checkbox"/>	Antibodies
<input type="checkbox"/>	Eukaryotic cell lines
<input checked="" type="checkbox"/>	Palaeontology and archaeology
<input checked="" type="checkbox"/>	Animals and other organisms
<input checked="" type="checkbox"/>	Human research participants
<input checked="" type="checkbox"/>	Clinical data
<input checked="" type="checkbox"/>	Dual use research of concern

Methods

n/a	Involved in the study
<input checked="" type="checkbox"/>	ChIP-seq
<input type="checkbox"/>	Flow cytometry
<input checked="" type="checkbox"/>	MRI-based neuroimaging

Antibodies

Antibodies used

anti-human CD56 APC (eBioscience), Cat# 17-0566-42 (1 : 500-1 : 1000 diluted)
 anti-GFP antibody (MBL), Cat#598 (1:500 diluted)
 anti-alpha1 Na/K ATPase antibody (Abcam), Cat# ab7671 (1:250 diluted)
 goat anti-mouse IgG cross-adsorbed secondary antibody, Alexa Fluor 633 (Invitrogen), Cat# A21052 (1:500 diluted)
 goat anti-rabbit IgG cross-adsorbed secondary antibody, Alexa Fluor 488 (Invitrogen), Cat# A11008 (1:500 diluted)

Validation

All the antibodies were validated.
 Anti-human CD56 APC was validated by the manufacturer applying for flow cytometry and for species including human, non-human

primate and Rhesus monkey.

Anti-GFP antibody was validated by the manufacturer for the following applications: Precipitation, Microscopy, ChIP, Electron Microscopy, Immunocytochemistry, Immunohistochemistry, Immunoprecipitation, and Western Blot. Species reactivity: Bovine, Canine, Chicken/avian, Donkey, Drosophila, Feline, Guinea pig, Hamster, Human, Mouse, Porcine, Rabbit, Rat, Sheep, Simian, Xenopus, Yeast.

Anti-alpha1 Na/K ATPase antibody was validated by manufacturer applying for Immunocytochemistry, Immunohistochemistry and western blot and for species including Mouse, Rat, Rabbit, Human, Pig.

Eukaryotic cell lines

Policy information about [cell lines](#)

Cell line source(s)

NRK (ATCC), CRL-6509™
Human MGC803, gift from Zhijie Chang laboratory, Tsinghua University, MGC-803 (RRID:CVCL_5334)
Mouse L929 (ATCC), CCL-1
YTS, gift from Zhongjun Dong laboratory, Tsinghua University, YTS (RRID:CVCL_D324)

Authentication

None of the cell line used have been authentication.

Mycoplasma contamination

The cell line were not tested for mycoplasma contamination.

Commonly misidentified lines (See [ICLAC](#) register)

No cell lines used in this study were found in the database of commonly misidentified cell lines that is maintained by ICLAC and NCBI Biosample

Flow Cytometry

Plots

Confirm that:

- The axis labels state the marker and fluorochrome used (e.g. CD4-FITC).
- The axis scales are clearly visible. Include numbers along axes only for bottom left plot of group (a 'group' is an analysis of identical markers).
- All plots are contour plots with outliers or pseudocolor plots.
- A numerical value for number of cells or percentage (with statistics) is provided.

Methodology

Sample preparation

MGC803 cells or their derivatives were co-cultured with YTS cells, and then for flow cytometry analysis

Instrument

Beckman CytoFlex LX was used to conduct related experiments

Software

Software of Beckman CytoFlex LX

Cell population abundance

around 10000~20000 MGC803 cells and ~150000 YTS cells for each sample

Gating strategy

Following the standard strategy of AnnexinV-PI cell death detection protocol.

- Tick this box to confirm that a figure exemplifying the gating strategy is provided in the Supplementary Information.